



NTNU – Trondheim
Norwegian University of
Science and Technology

Diatoms in new design

Markus Morland

Mechanical Engineering

Submission date: June 2014

Supervisor: Christian Thaulow, IPM

Norwegian University of Science and Technology
Department of Engineering Design and Materials

THE NORWEGIAN UNIVERSITY
OF SCIENCE AND TECHNOLOGY
DEPARTMENT OF ENGINEERING DESIGN
AND MATERIALS

**MASTER THESIS 2014
FOR
STUD. TECHN. MARKUS MORLAND**

DIATOMS IN NEW DESIGN

Nytt design inspirert av kiselalger

A variety of potential applications for diatom frustules have been proposed and explored in the literature. This includes optics, photonics, catalysis, nanofabrication, biosensing, drug delivery, filtration and bioencapsulations. Most of these applications rely on using the unique and ordered porous structures of the frustule valves. The material properties of pores provide a large scope for exploitation, for example used for separation processes and within microfluidic channels for filtering, trapping and sorting nanoparticles.

The mechanical properties of the frustules are unique. Clearly the frustules have evolved to withstand external pressure and considerable energy and specialized tools are required to break them. The frustule is effective armour against many potential predators.

The candidate shall

- 1) present a range of potential applications of diatom frustules and discuss further developments
- 2) discuss the material mechanical properties with special focus on the effects of ‘holes and spheres
- 3) develop “Diatom inspired design”, where mechanical and functional properties can be utilized
- 4) if time permits fabricate diatom-based specimens at NTNU Nanolab and perform testing at NTNU Nanomechanical lab

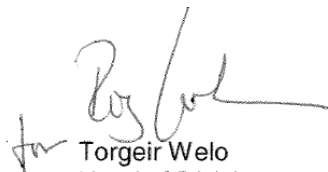
Three weeks after start of the thesis work, an A3 sheet illustrating the work is to be handed in. A template for this presentation is available on the IPM’s web site under the menu “Masteroppgave” (<http://fwww.ntnu.no/ipm/masteroppgave>). This sheet should be updated one week before the Master’s thesis is submitted.


Performing a risk assessment of the planned work is obligatory. Known main activities must be risk assessed before they start, and the form must be handed in within 3 weeks of

receiving the problem text. The form must be signed by your supervisor. All projects are to be assessed, even theoretical and virtual. Risk assessment is a running activity, and must be carried out before starting any activity that might lead to injury to humans or damage to materials/equipment or the external environment, Copies of signed risk assessments should also be included as an appendix of the finished project report.

The thesis should include the signed problem text, and be written as a research report with summary both in English and Norwegian, conclusion, literature references, table of contents, etc. During preparation of the text, the candidate should make efforts to create a well arranged and well written report. To ease the evaluation of the thesis, it is important to cross-reference text, tables and figures. For evaluation of the work a thorough discussion of results is appreciated.

The thesis shall be submitted electronically via DAIM, NTNU's system for Digital Archiving and Submission of Master's thesis.


Torgeir Welo
Head of Division


Christian Thaulow
Professor/Supervisor



“Science may set limits to knowledge, but should not set limits to imagination”

- Bertrand Russell

Preface

One might be forgiven for thinking that we, as a species, have reached the pinnacle of technology – especially considering that many now have more computing power on their mobile phones than NASA needed to send people into space – but this is simply not the case. Scientists and engineers have often looked to nature for inspiration and for solutions to specific problems, and as technology progresses our ability to observe finer detail in nature progresses along with it.

This thesis was to consist of three parts. However, due to time limitations, my supervisor and I agreed to disregard the third part of the thesis. The focus of this thesis will be on the material properties of diatom silica.

I would like to thank my supervisor Prof. Christian Thaulow, whose door was always open, for encouragement and guidance. I would also like to thank the study group led by Håkon Gundersen for valuable feedback and discussions. Lastly, a big thank you to Nana for all the support.

Markus Morland

Abstract

The first part of this thesis is a literature study into the applications of diatom frustules. The second part is FE-analysis of micromechanical testing of diatom frustules undertaken at NTNU. The models are based on SEM-images of the specimens before and after testing. The simulations are initially run under an assumed young's modulus, the young's modulus is then modified until the displacement of the real and virtual tests yield identical results. Two distinct tests are analyzed in this thesis, a cantilever bending test (CBT) and a three-point bending test (TPBT), both on *Coscinodiscus* sp. frustules.

The simulations of the CBT and TPBT returned young's moduli of 32.8GPa and 36.7GPa, respectively. The returned values for stress varied on the mesh size being used, a mesh size of the 10mm – equivalent to 10nm – returned 3415MPa and 2690MPa for the CBT and TPBT respectively. However, the point of highest stress in the TPBT simulation does not coincide with the fracture in the specimen.

Since the results presented in this thesis are based on only two models, the dataset is insufficient to draw any conclusions as to the mechanical properties of the material. Further mechanical tests should be performed, with the purpose of analyzing the results using FE-tools. By documenting the geometry of the specimens thoroughly prior to testing, more accurate models can be made.

Sammendrag

Den første delen av masteroppgaven er en litteraturstudie på eksisterende bruksområder for frustuler til diatomeer. Den andre delen av masteroppgaven er en FE-analyse av mikromekanisk testing av diatome frustuler utført ved NTNU. Modellene er basert på SEM-bilder av prøvene før og etter testingen ble utført. Simuleringene ble først kjørt med en antatt elastisitetsmodul, som senere ble modifisert inntil forskyvningen av den ekte og virtuelle testen ga identiske resultater. To separate tester er analysert i oppgaven, en cantilever bøyetest (CBT) og en tre-punkt bøyetest (TPBT), begge utført på *Coscinodiscus* sp. frustuler.

Simuleringene fra CBT og TPBT ga elastisitetsmoduler på henholdsvis 32.8GPa og 36.7GPa. De returnerte verdiene for spenning varierte avhengig av finheten på elementnettet som ble benyttet. Et elementnett på 10mm – ekvivalent til 10nm – resulterte i spenninger på 3415MPa and 2690MPa for henholdsvis CBT og TPBT.

Da resultatene i denne oppgaven er basert på bare to modeller, er det for lite data tilgjengelig for å komme med en reell konklusjon hva angår materialets mekaniske egenskaper. Flere mekaniske tester må gjennomføres med FE-analyse som mål. Ved å dokumentere geometrien til prøven før testing, kan man lage mer nøyaktige modeller.

Contents

Preface	v
Abstract	vi
Sammendrag	vii
1. Introduction	1
2. Potential applications for diatom frustules	3
2.1 Medical applications	3
2.1.1 Biosensors	3
2.1.2 Drug delivery	4
2.2 Filtration	5
3. FE-analysis of previous mechanical testing	6
3.1 Literature study	6
3.2 Mechanical testing at NTNU	8
3.3 Methods and materials	11
3.3.1 Geometry and load scaling	11
3.3.2 Modelling	11
3.4 Simulation procedure	13
3.4.1 Cantilever bending test	13
3.4.2 Three-point-bending test	15
3.4.3 Determining material properties	19
3.4.4 Mesh size and refining	19
3.4.5 Parameter study	19
3.5 Results	21
3.5.1 Cantilever bending test	21
3.5.2 Three-point-bending test	23
3.5.3 Convergence	26
3.6 Discussion	27
3.6.1 Cantilever bending test	27
3.6.2 Three-point-bending test	27
3.6.3 Young's modulus	28
3.6.4 Ultimate strength	28
3.7 Conclusion	29
3.8 Further work	29
Referances	30
Appendix A - Scaling of geometry and loads	I

A.1	Normal stress and shear stress	I
A.2	Bending stress.....	I
Appendix B	- Modelling of Bjørnøy's H ₂ O ₂ Beam 7	II
Appendix C	- Modelling of the Cantilever Beam Test Specimen.....	IV

1. Introduction

3.5 billion years ago, the first single-cell organisms started moving around in the oceans. Since then, every life form has spent their time uniquely adapting to their surroundings. In the case of diatoms, which evolved about 180 million years ago[1], this adaptation resulted in a glass exoskeleton capable of protecting the organism from predators[2].

Diatoms are photosynthetic algae that live in both seawater and fresh water, wherever enough light and nutrients are found. This group of phytoplankton is estimated to comprise more than 200 000 living species, varying in size from 2µm to 2mm[3]. Diatoms are estimated to contribute up to 25% to the world primary production of organic carbon, capturing carbon dioxide (CO₂) and sunlight to sustain themselves, and releasing oxygen in the process[4].

What separates them from other phytoplankton groups is their ability to form a rigid outer cell wall, termed a frustule illustrated schematically in Figure 1, made of amorphous hydrated silica - SiO₂ * 2 H₂O[1].

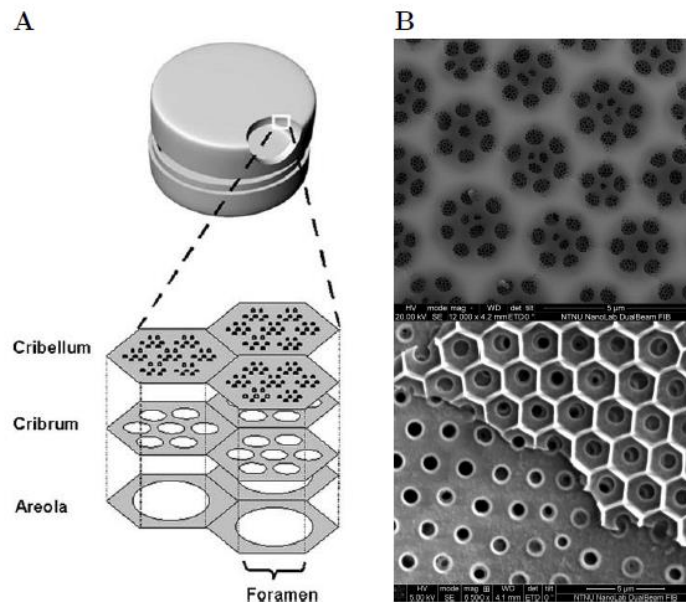


Figure 1: A) schematic drawing of the cross-section of the frustule reproduced from Losic et al.[5] illustrating the layers from bottom to top; Aerola, Cribrum and Cribellum and B) SEM-images of the structure of the Coscinodiscus sp. diatom taken from Sindre H. Bjørnøy[6]. The top two layers of the frustule; cribellum and cribrum, are visible on the top SEM-image, while the areola and the foramen are illustrated in the bottom SEM-picture.

The purpose of this frustule is debated; however, one theory is that the frustule serves as armor to protect the organism from predators. A large variety of organisms feed on diatoms, so any measure that reduces mortality would be an effective first line of defense[2].

Diatoms are divided into two orders based on the shape of the frustule: Centrales and Pennales. These orders comprise round and elongated diatoms, respectively. Centric diatoms are radially and bilaterally symmetric, whereas pennate diatoms are bilaterally symmetric. This symmetry has given rise to the group name diatoms, from the Greek diatomos, meaning cut in two[7].

Diatoms generally reproduce asexually, and can do so up to 8 times per day. Asexual division, however, reduces the average size of the population over time[2, 4]. After a number of divisions, the cell will resort to sexual reproduction, and a spore is created. This spore will form a fully-grown diatom, and the cycle will begin again[7].

2. Potential applications for diatom frustules

Diatoms have several characteristics that may make them well suited for a range of applications – from medical uses for drug delivery and in biosensing arrays to industrial filters. In this section, a range of potential applications is presented, as well as their benefits.

2.1 Medical applications

2.1.1 Biosensors

A biosensor is a device used to confirm the presence of a specific biological substance in a sample. Some medical conditions may be diagnosed rapidly by detection of certain biomarkers in samples collected from the patient. Smaller, cheaper biosensors with higher sensitivity could provide third-world nations with a reliable method of diagnosing diseases on site.

Some medical conditions may be diagnosed rapidly by detection of biomarkers in samples obtained from the patient. A study by H. E. Townley et al. demonstrates that the large surface area of the diatom *Coscinodiscus wailesii* can be utilized in biosensors to detect specific secondary antibodies[8]. Primary antibodies were tethered to the surface of the diatom, which was then incubated with secondary antibodies. The presence of secondary antibodies was confirmed using confocal microscopy. It was also demonstrated that two separate antibodies can be tethered to the same frustule, retaining specificity.

A study by K.-C. Lin et al., also utilizing *C. wailesii* frustules, describes a similar process to detect two proteins associated with acute coronary syndrome in human serum[9]. Using a gold electrode to measure the change in capacitance associated with protein-binding events, they reported enhanced response time, dynamic range, signal strength, sensitivity and selectivity.

In a recent study, a highly sensitive biosensor was made by using small diatoms, *Nitzschia soratensis*, as the membrane while using a second, much larger diatom, *Coscinodiscus argus* as a filter[10].

2.1.2 Drug delivery

Drug delivery is a method, or a process, where pharmaceutical compounds are being administered to achieve a medical effect in humans or animals. In recent years, synthetic silica has been widely used when developing new drug delivery systems. This because they have traits such as; excellent biocompatibility, large surface area, thermal stability, chemical inertness and controlled diffusion mechanism which may be utilized. Although this has been very useful, synthetic silica has disadvantages. Silica synthesis is time consuming, costly, involves high-energy consumptions and toxic materials are being used. Hence, alternative methods for acquiring silica has been investigated, and diatoms has been one of the solutions[4]. The diatoms has a unique frustule that surrounds the cell and consist of silica generated biologically by the algae[4, 11].

By using diatom frustules, one may be able to overcome some of the difficulties associated with localized drug delivery, such as poor cellular penetration and degradation of small molecules. Diatoms have been suggested as a substitute for other drug-delivery vehicles due to structural, mechanical, chemical and optical characteristics that might overcome these difficulties. Additionally, diatoms have a large surface area, exhibit nanoscale porosity and are biocompatible and biodegradable[11].

Losic et al. demonstrated that diatom frustules can be functionalized with dopamine modified Fe_3O_4 particles, making them magnetic. This property allowed the researchers to control the motion of the particles with an external magnetic field. They also confirmed that the dopamine amino groups were active and available for the attachment of targeting ligands[12].

While being able to control the motion of the particles is promising, the prospect of self-propelled nanomachines is one that has titillated scientists and science-fiction writers for decades. This may be achieved by attaching a bacteria to the frustule. Many bacteria propel themselves by rotating corkscrew-like with tails termed flagella. Behkam & Sitti demonstrated this effect by using *Serratia marcescens* bacteria to propel polystyrene beads[13]. By adding copper ions (Cu^{2+}) and ethylenediaminetetraacetic acid respectively, they were able to stop and resume the flagellar motion. The rate of motion for the polystyrene beads were up to 100 times those of diffusion alone, showing that the beads were indeed propelled by the bacteria.

2.2 Filtration

Diatom frustules have several applications as micro- and nanoparticle filters, owing to the pores in their frustules. The size and distribution of these pores are specie-specific, e.g. the related species *Melosira nyassensis* and *M. nummolooides* have 6-8 pores and 16-25 pores per 10µm, respectively. In addition to variations between species, variations in temperature and the concentrations of salt and germanium may influence pore size in a population[4]. By carefully controlling the production environment, one could select for a range of discrete pore sizes. Some species of diatoms reproduce asexually up to 8 times per day [4, 7], so a large quantity of algae can be grown rapidly, allowing for industrial applications.

As discussed earlier, diatom frustules may be used as filters to avoid false positives in biosensors, filtering out larger particles that would otherwise disrupt the signal.

3. FE-analysis of previous mechanical testing

In this section, mechanical testing previously undertaken at NTNU is evaluated using FE-tools. The purpose of this analysis is to determine the young's modulus and ultimate strength of the diatom silica. Various studies have studied these properties and, as will be shown, have reported widely varying results, both in terms of strength and elasticity of the diatom silica.

3.1 Literature study

In 2001, Almqvist et al used nanoindentation to determine the hardness and elasticity of the frustules of the species *Navicula pelliculosa* [14]. They reported widely varying results depending on the exact position on the frustule. Elasticity varied from 1-12 GPa, and hardness varied from 7 to hundreds of GPa.

In 2003, Hamm et al used calibrated borosilicate glass microneedles to load and break diatom frustules[2]. Their hypothesis was that the frustule serves as armor, protecting the organism from predators. Three species of diatoms were tested: the centric species *Thalassiosira punctigera*, the much larger *Coscinodiscus granii* and the pennate diatom *Fragilariopsis kerguelensis*. They found that remarkably large forces were required to break the frustules, up to 700 tonnes m^{-2} . They also reported an inverse relationship between the size of the frustule and the force required to break it. This inverse relationship was present not only within a species, but also between different species.

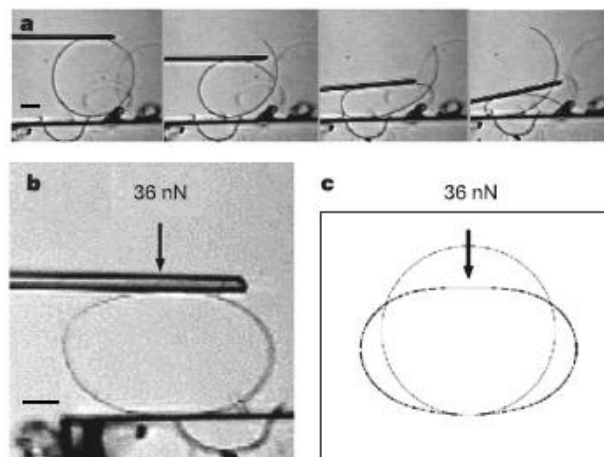


Figure 2: Properties of an isolated girdle band. a: sequence showing deformation with increasing force. b: girdle band (pleura) deformed by a calibrated glass needle. c, FEM of the pleura, showing identical deflections as functions of the same force (36 nN). The Young's modulus E of the silica in the FEM is 22.4 GPa. Scale bars, 10 μm . Reproduced from Hamm & Merkel (2003)

As shown in Figure 2, reproduced from Hamm et al(2003), a closed pleura was used to determine the young's modulus of the diatom silica. By loading the FE-model under an assumed young's modulus, deformation as a function of force could be calculated, and the young's modulus modified until the test and simulation yielded identical results. With this approach, they determined the young's modulus to be 22.4 GPa.

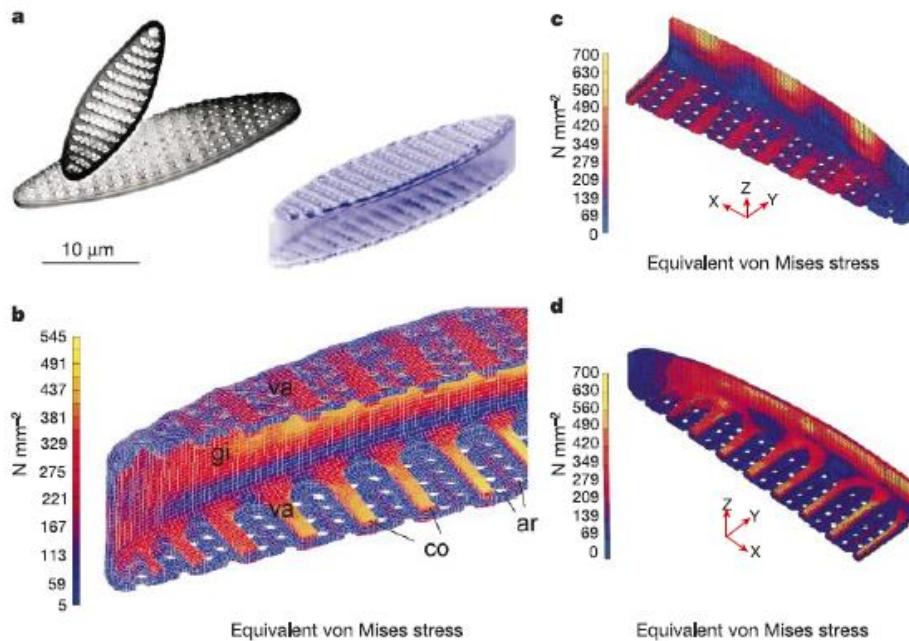


Figure 3: FE-simulation of the *F. kerguelensis* frustules. a: SEM of two valves (left) and rendered FEM of a complete frustule (right). b: Equivalent von Mises stress within the frustule as a function of pressure (total force, 750 mN) on the girdle region. gi, girdle region; va, valve; co, costae; ar, areolae. c, d: One-eighth sections, external (c) and internal (d) views. Equivalent von Mises stress caused by pressure applied on several spots (area of each spot, 1 mm²; total force, 750 µN), simulating a mandible bite; stress is absorbed by the costae. Image and caption reproduced from Hamm & Merkel (2003).

To determine the strength of the silica, they analyzed the *F. kerguelensis* frustule using FE-tools. To simulate a mandible bite, a load of 750µN was applied to the girdle region. As shown in Figure 3, reproduced from Hamm & Merkel (2003), the forces were largely absorbed by the costae. The findings of Hamm & Merkel indicate an ultimate strength of the diatom silica in excess of 540N mm⁻¹.

They also noted that the apparent lack of plastic deformation, indicating that the diatom silica is a brittle material, is consistent with the sharp-edged and smooth fracture sites found in broken frustules.

3.2 Mechanical testing at NTNU

In 2011, S. H. Bjørnøy developed a novel approach to nanomechanical testing of diatom frustules[6]. *Coscinodiscus* frustules were treated with one of three different chemical solutions: sodium dodecyl sulphate (SDS), sulphuric acid (H_2SO_4) and hydrogen peroxide (H_2O_2). The difference between these treatments is the amount of organic matter removed from the frustules prior to testing.

Beams were milled from the samples using a DualBeam FIB, and were then transferred to the sample holder. To position the indenter tip accurately in the center of the beam, the indenter was used to scan the surface of the specimen. In the initial testing, the beams were lying freely in the sample holder. However, during the scanning procedure the indenter tip removed 50 % of the samples. To prevent this, the samples were attached to the sample holder using a small amount of deposited platinum. These attachments were to be strong enough to prevent the scanning tip from removing the sample, but weak enough to allow the beam to settle in the sample holder during indentation.

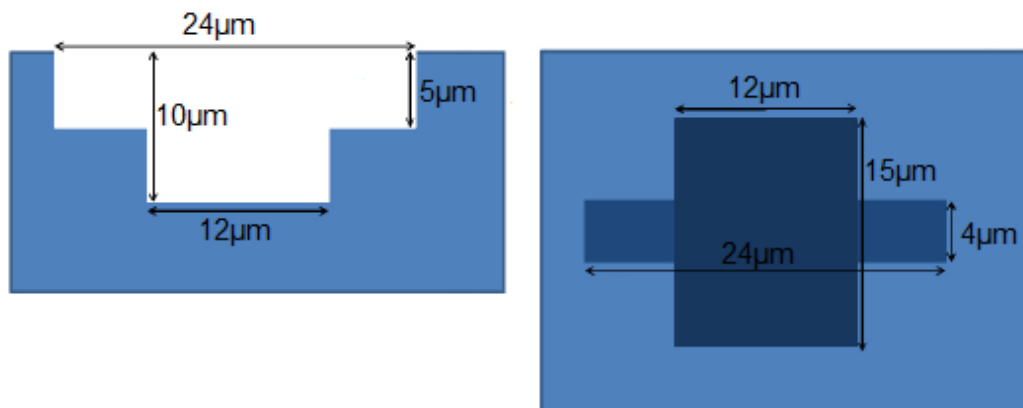


Figure 4: Schematic side view (left) and top view (right) of the sample holder developed and used by S.H. Bjørnøy. Adapted from S.H. Bjørnøy's master thesis.

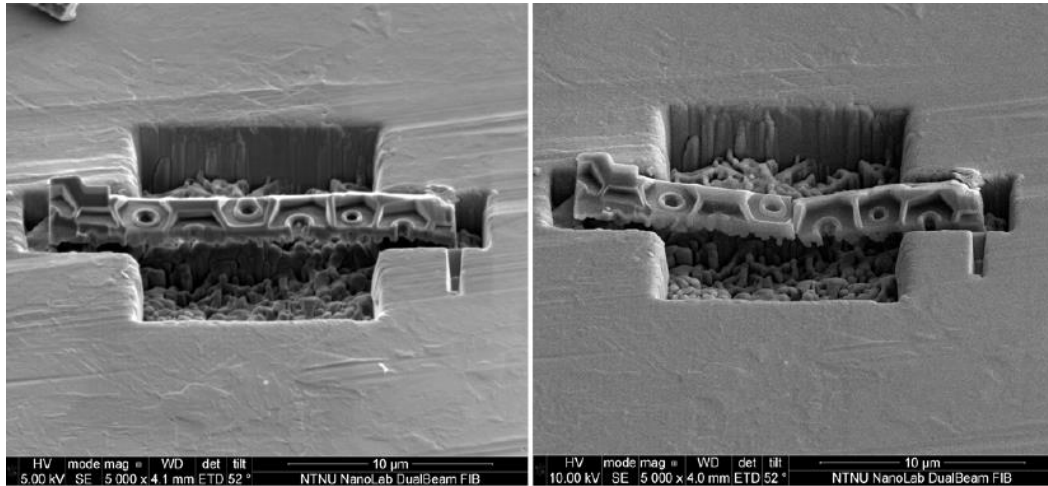


Figure 5: SEM-images of the “H₂O₂ Beam 7” before and after testing. The beam is viewed at a 52° angle. Image adapted from S. H. Bjørnøys master thesis.

Using this procedure, it was shown that the diatom silica is a highly brittle material with a fracture strength of 336 ± 73 MPa and a flexural modulus of 5.72 ± 2.9 GPa. It was also noted that the samples from frustules cleaned with the mildest chemical treatment, SDS, fractured at lower strains than the other samples.

At the conclusion of his master’s thesis, Bjørnøys suggest a different approach to mechanical testing, illustrated in Figure 6.

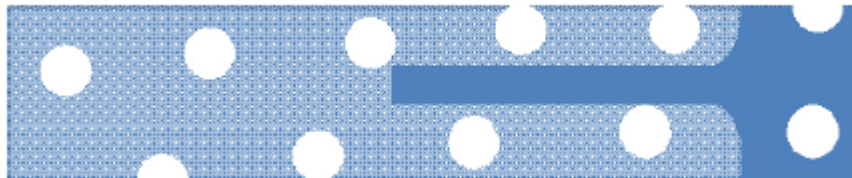


Figure 6: A schematic drawing of the proposed beam configuration. A comparison to the beams used by Bjørnøys is shown. Image reproduced from S. H. Bjørnøys master thesis.

By milling a smaller beam from an area of the frustule without pores, it would be possible to machine a beam with a constant, massive cross section, making evaluating the results easier.

In 2012, M. J. Vebner continued the work of S. H. Bjørnøys, and determined that the three-point bending test involved too many uncertainties[15]. Instead of moving the beams to a separate sample holder, the beams were to be tested while attached to the frustule. As proposed by Bjørnøys, the beams were machined from a part of the frustule without pores,

making for simpler evaluation after testing. 21 beams were successfully produced, but as this approach had not been attempted previously, no successful bending tests were performed.

The results of the tests attempted by M. J. Vebner formed the basis for two successful bending tests performed by Prof. Christian Thaulow. The results of one of the tests can be seen in

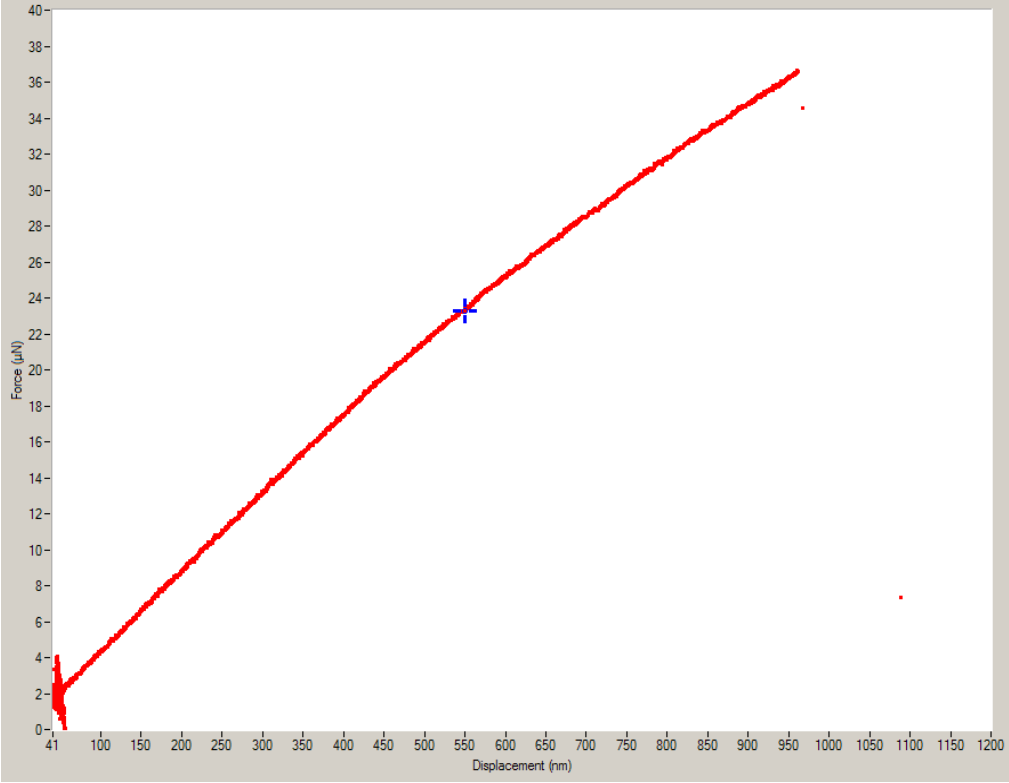


Figure 7: Output data from the cantilever bending test performed by Prof. Christian Thaulow.

3.3 Methods and materials

3.3.1 Geometry and load scaling

A minor limitation in Siemens NX is that the program will not consider a nanoscale sketch to be valid geometry. To avoid this problem, the model was scaled up by a factor of 10^6 , i.e. nanometers were modelled as millimeters. Subsequently, the loads were scaled up by a factor 10^{12} . Detailed calculations regarding the validity of this scaling are presented in appendix A.

3.3.2 Modelling

When creating the 3D-models of the test specimens, the goal was to model the geometry as closely as possible. The models are based on measurements from SEM-images from S. H. Bjørnøy's master thesis (SIT K/L) and images supplied by Christian Thaulow. Side by side comparisons of the models and specimens are shown in Figure 8 and Figure 9.

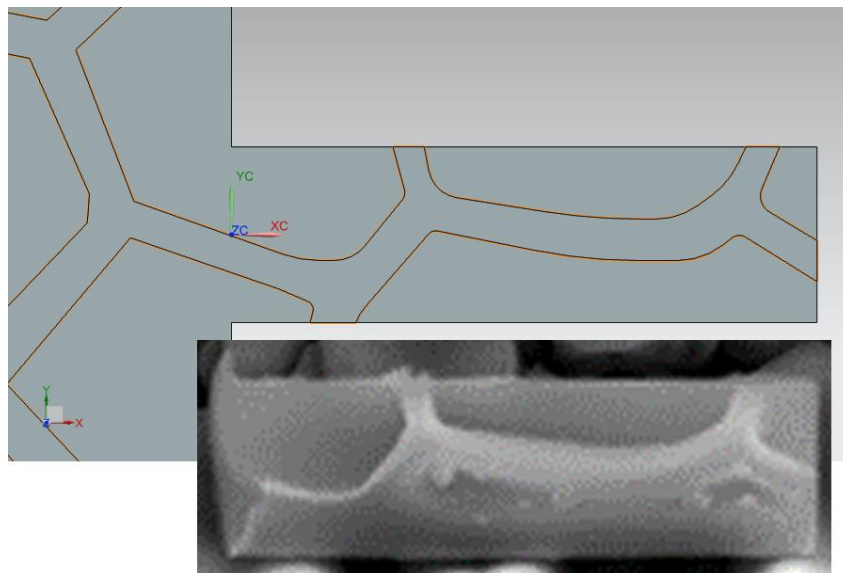


Figure 8: Side by side comparison of the fractured CBT beam and the corresponding geometry of the model

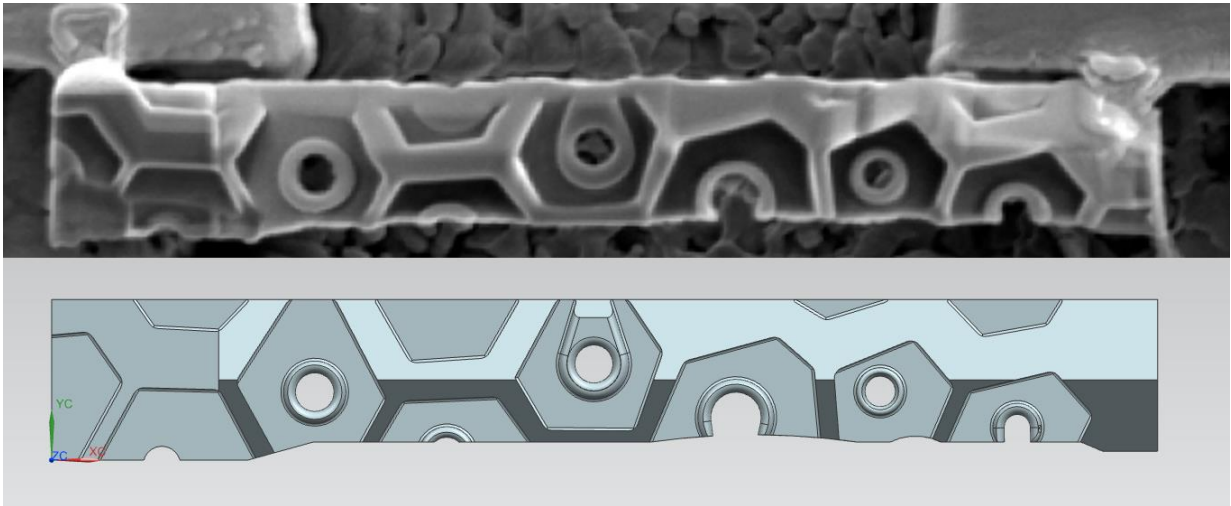


Figure 9: Side by side comparison of the TPBT beam before testing and the FE-model

The process is described in detail in appendages B and C.

3.4 Simulation procedure

In this section, details of the simulation procedures and parameters chosen are described.

3.4.1 Cantilever bending test

The initial simulations on the cantilever bending test involved constraining the model by a semicircular disc at the fixed end. This approach turned out to be suitable only to assess the stresses in the beam, and provided no useful information as to the elasticity of the material. The simulations yielded vastly varying young's moduli depending on the radius of the disc. The model shown in Figure 10 includes a disc with radius equal to the width of the beam.

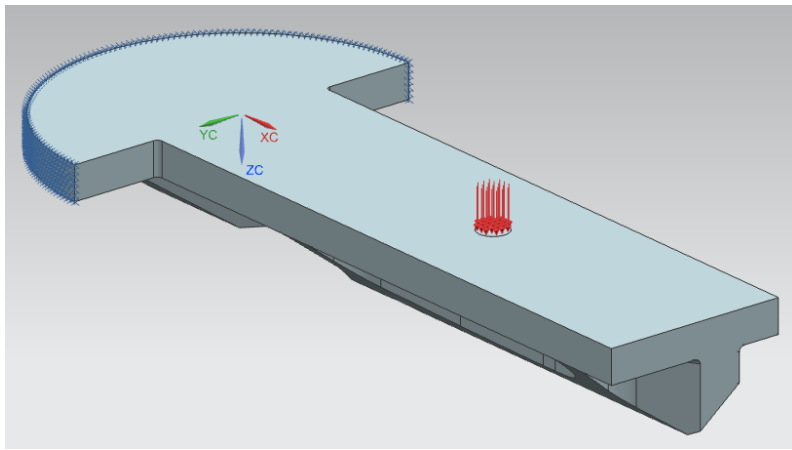


Figure 10: Cantilever bending test model with semicircular disc for constraint. The radius of the disc is equal to the width of the beam.

To establish a lower limit for the young's modulus, the simulation was run without any supporting structure, constraining the model approximately where the beam joins the frustule.

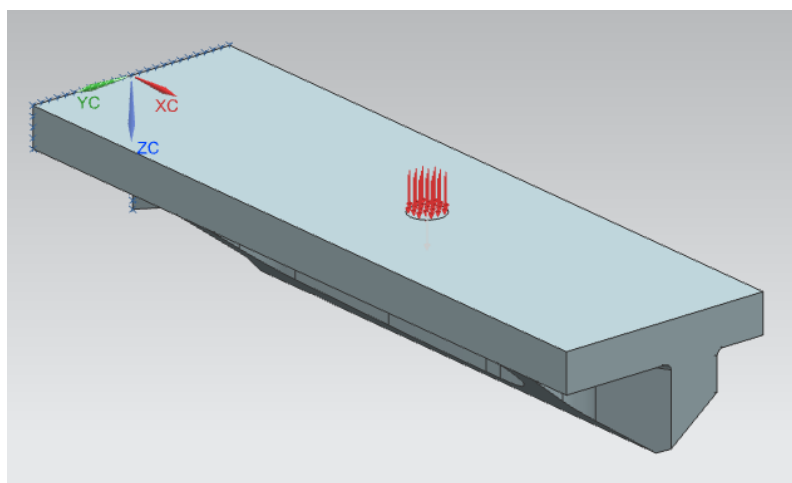


Figure 11: Cantilever bending test simulation without supporting structure, to determine the lower limit of the young's modulus.

To more accurately simulate the deformation in the supporting structure, it was decided to include in the model a part of the surrounding frustule. Based on the SEM-images provided by Christian Thaulow, the foramen and cribrum layers appear to be approximately the same thickness. The process involved in modelling the supporting structure is described in appendix (appendagesd). The supporting structure shown in Figure 12 measures two by five times the width of the beam.

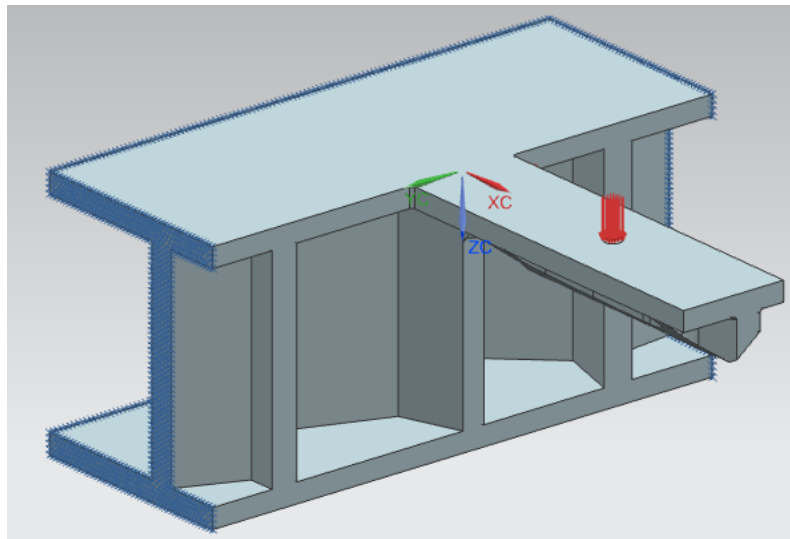


Figure 12: Cantilever bending test model with supporting structure.

To place the load, a minor feature was added to the model, serving as a reference point. The distance along the beam to the placing of the load, 3300nm, was provided by Prof. Christian Thaulow. The applied load is 38MN.

In the initial simulations, the highest stresses were recorded in one of the corners joining the beam to the supporting structure. Comparing these findings to the images provided by Prof. Christian Thaulow, it was apparent that the fracture started in this corner. As illustrated in Figure 13, the fracture coincides with the corner indicated by the arrow, and circumnavigates the opposing corner.

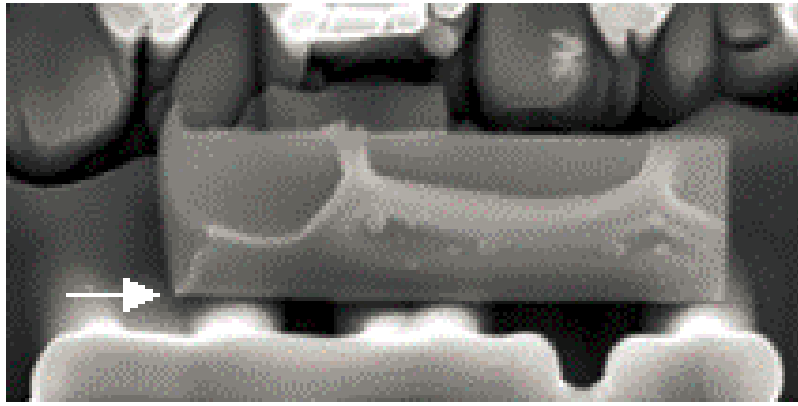


Figure 13: SEM-image of the fractured cantilever beam. The arrow indicates the point where the fracture is assumed to have initiated. Image courtesy of Prof. Christian Thaulow.

Hence, the mesh was refined in the corner indicated by the arrow in Figure 13. Figure 14 illustrates the refined mesh surrounding the corner.

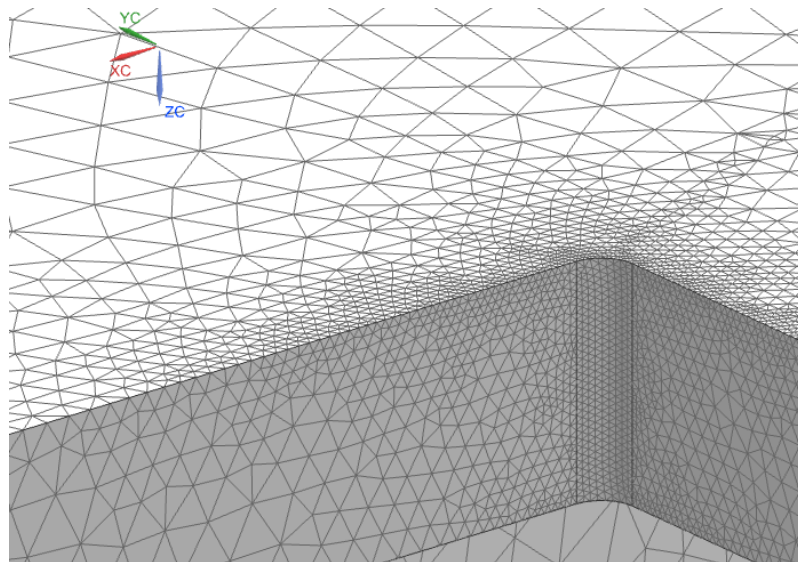


Figure 14: Mesh surrounding the corner where the crack is assumed to have originated. Local mesh size 10mm, global mesh size 150mm. The coordinate axes indicate the center of the beam.

3.4.2 Three-point-bending test

The TPBT model was constrained using two minor features added to the underside of the model. These features served as reference lines ensuring a predictable behavior of the constraints. As the supporting edges of the sample holder developed by S. H. Bjørnøy were 12 μ m apart, these features were modelled 12 000mm apart.

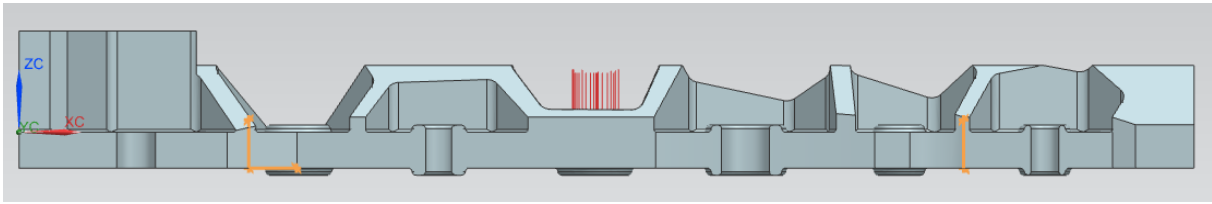


Figure 15: Side view of the TPBT model, the constraints are highlighted. The left constraint allows rotation, but no translation. The right constraint allows longitudinal translation as well as rotation.

Figure 15 shows a side view of the TPBT model, the constraints are highlighted. To accommodate for the deflection of the beam, the constraints were after the initial simulations moved slightly further apart. The constraint on the left allows rotation, but no translation. The constraint on the right, however, allows translation along the length of the beam. After the initial simulations, the longitudinal deflection of the constrained edge was added to the distance between the constraining features. This way, the distance between the constraints remained 12 000mm at maximum deflection.

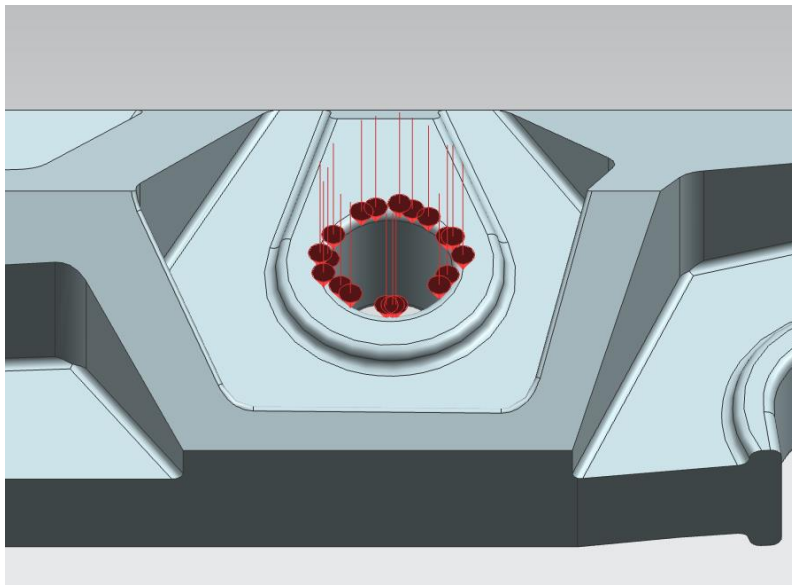


Figure 16: The load is placed on the inside curvature of the lip. The load is 60.144MN.

To load the model, a force of 60.144 MN was applied to the inner radius of the lip, as shown in Figure 16. This location does not coincide with the centers of the beam or sample holder. However, Bjørnøy describes using a conical tip with a radius of 600nm in his testing. An indenter tip with that geometry would have collided with the areola layer before contacting the foramen layer. Figure 17 shows an assembly of the TPBT model and an indenter tip with the geometry used by S. H. Bjørnøy. The red color indicates overlap between the parts. It is therefore assumed that the indenter will have slid into the pore during loading.

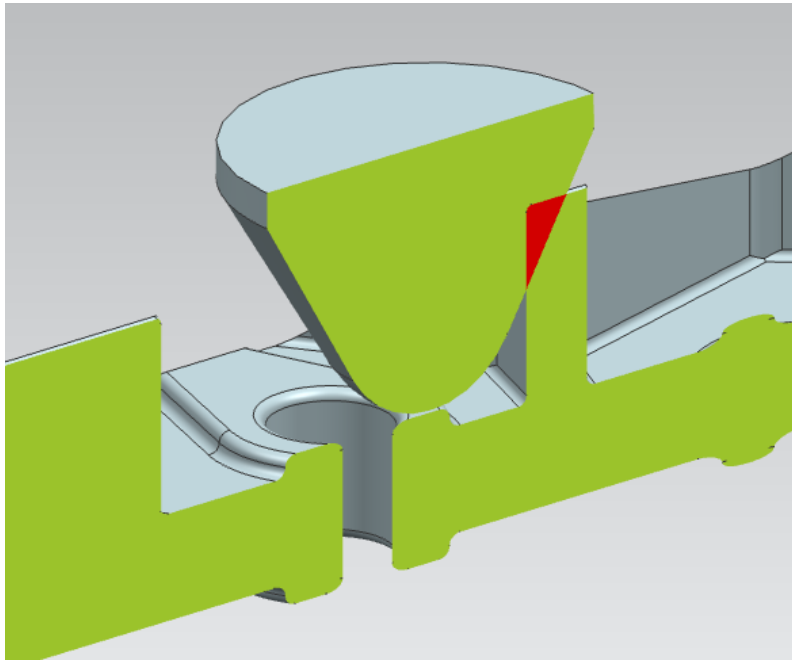


Figure 17: Section view of an assembly of the TPBT model and a model of the indenter tip. The red area illustrates the overlap between the parts.

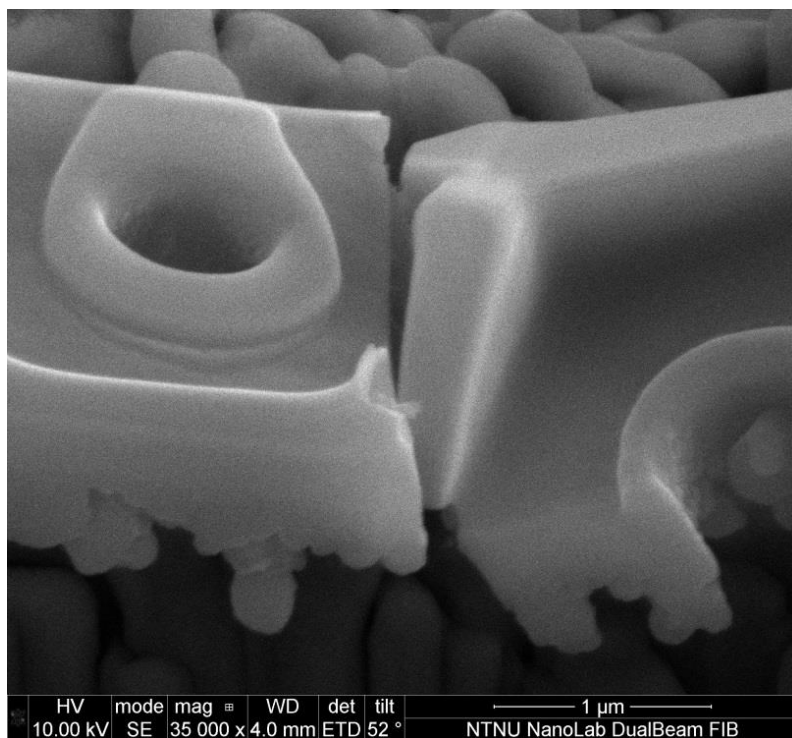


Figure 18: SEM-image of the fractured " H_2O_2 Beam 7", the beam is viewed at a 52° angle.

Figure 18 shows the fractured TPBT specimen, illustrating the position of the fracture.

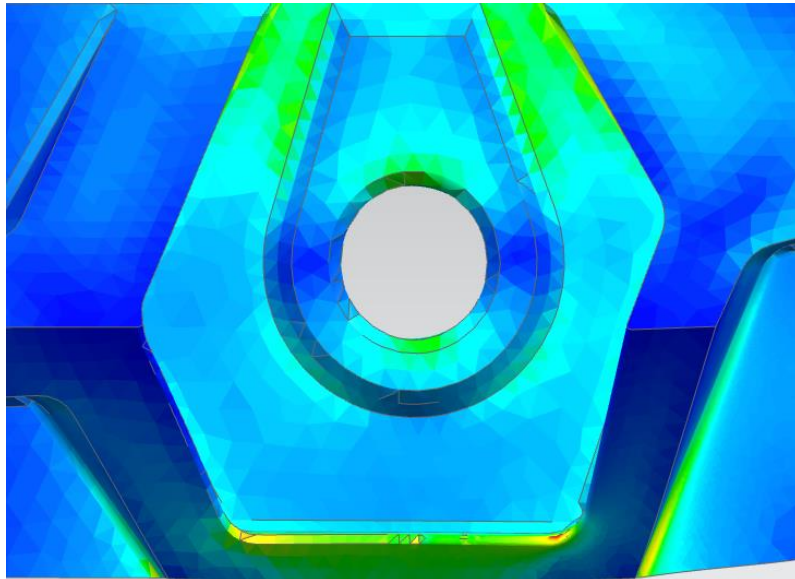


Figure 19: Top view of the stress results, showing stress distribution in the same area as illustrated in Figure 18. The highest stresses do not coincide with the fracture in the specimen.

Comparing Figure 18 and Figure 19, it is apparent the highest stresses in the model do not coincide with the fracture in the specimen. However, the stresses presented in the results are recorded in the area shown in Figure 20.

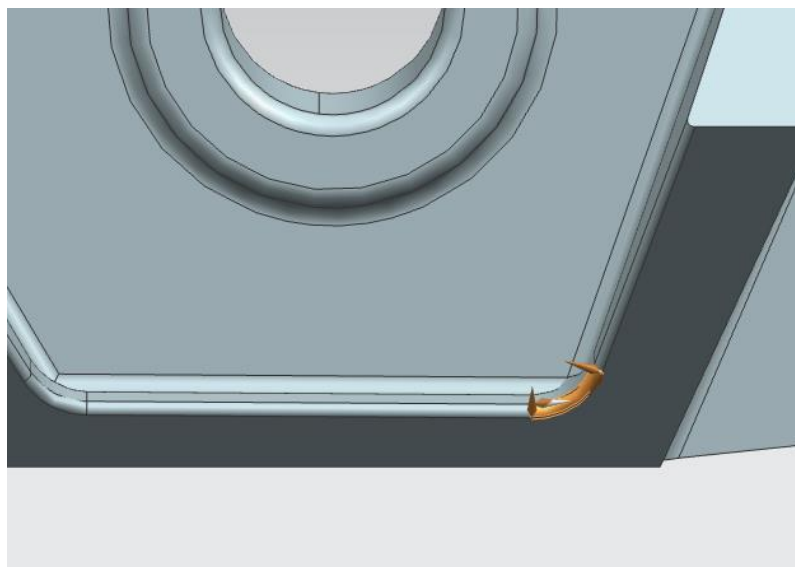


Figure 20: Top view of the TPBT model. The highlighted area shows the area where the mesh was refined to 10mm. The stresses presented in the results are recorded in this area.

3.4.3 Determining material properties

Since the young's modulus of the material is unknown, the simulations were first run under an assumed young's modulus. By comparing the deformation in the simulation to the test, the young's modulus was modified until the simulations and mechanical tests yielded identical results. The target deformation for the CBT was 960mm, and 804mm for the TPBT.

By reading the deformation in the loaded area, the corrected young's modulus could then be calculated:

$$E_{Corr} = E_{Ass} * \frac{Actual\ deformation}{Expected\ deformation} \quad (1)$$

The simulation was then run again with the corrected young's modulus, and the deformation confirmed. When the physical test and simulation yields identical results, the stress can be read from the simulation. This procedure is similar to the one described by Hamm et al[2].

3.4.4 Mesh size and refining

All simulations were run with a global mesh size of 150mm, and a local mesh size of 10mm where the highest stresses are recorded. The element type is TET10, 10 node tetrahedral elements. An attempt was made to refine the mesh until the values for stress would converge. However, the values did not converge as will be discussed later, and a mesh size of 10mm was used.

3.4.5 Parameter study

To better understand how the thickness of the foramen and areola layers influence the properties of the specimens, a parameter study was performed on both models. This parameter study also illustrates the properties of the specimen, should the measurements prove to be inaccurate. This was done by varying the thickness of the foramen and areola layers independently.

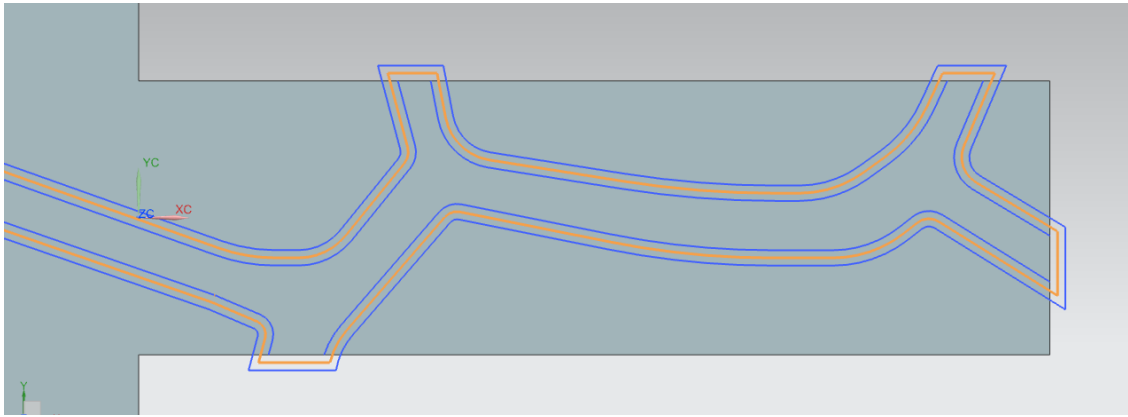


Figure 21: The outline of the areola layer in the CBT-model. The original outline is highlighted. On either side, the offset outline is shown. The offset is $\pm 50\text{mm}$.

Figure 21 illustrates the three different thicknesses of the areola layer in the CBT model. The thickness of the foramen layer, as provided by Christian Thaulow, was 310-350nm. In the parameter study, simulations were run with thicknesses 310mm, 330mm and 350mm, combined with no offset, -50mm offset or +50mm offset of the areola.

Since the foramen layer of the TPBT was substantially thicker than on the CBT, the thickness was varied more in this study. Simulations were run with the thicknesses 560mm, 600mm and 640mm. The range of offsets on the areola layer was identical. Figure 22 illustrates the different sizes of the areola layer in the TPBT model.

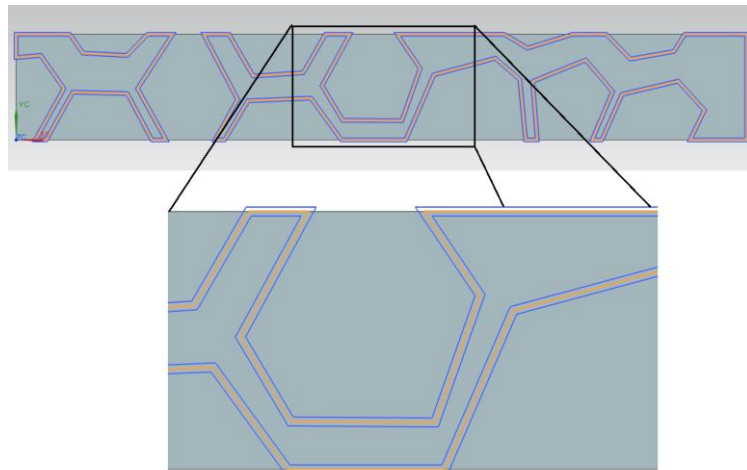


Figure 22: The outline of the areola layer in the TPBT-model. The original outline is highlighted. On either side, the offset outline is shown. The offset is $\pm 50\text{mm}$.

3.5 Results

In this section, the results of the simulations are presented. Brief explanations are given in this section, but the discussion is kept to a minimum. The results are thoroughly discussed in the next sections.

3.5.1 Cantilever bending test

In the simulations of the CBT, the young's modulus was found to be 32.8GPa. (insert lower limit figures)

In the course of the parameter study on the cantilever bending test, the calculated young's moduli varied from 24.1GPa to 48.1GPa, as seen in Table 1.

Young's modulus [MPa]

Table 1: Results of the cantilever bending test simulations, showing the young's modulus as the thickness of the areola and foramen layers is varied. Units are MPa, mesh size is 10mm.

Young's modulus [MPa]	Foramen thickness		
	310mm	330mm	350mm
Areola offset			
-50mm	48053	43667	39795
0	35712	32845	30257
+50mm	27975	25937	24086

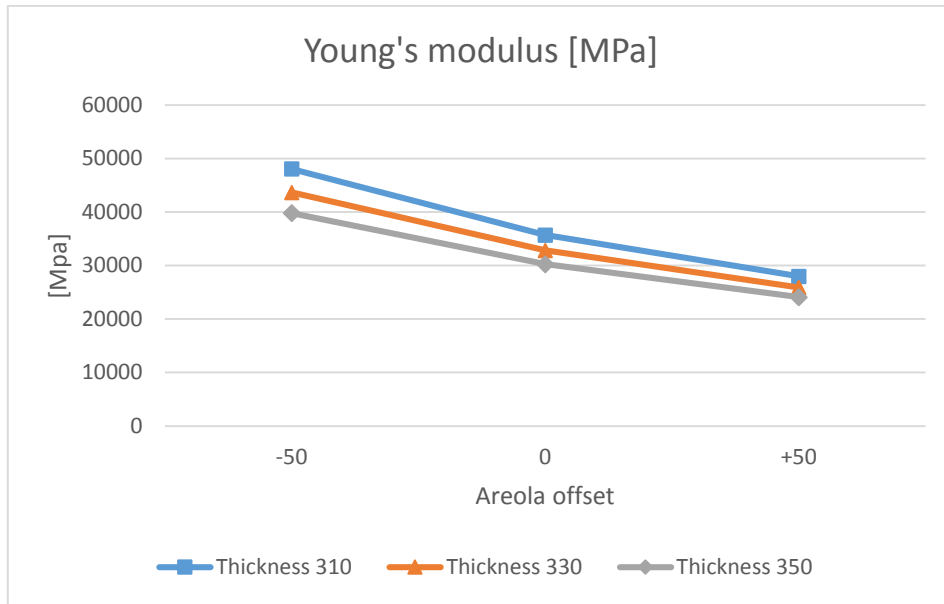


Figure 23: Graphical representation of the data in Table 1, showing the calculated young's modulus of the cantilever bending test specimen as the thickness of the areola and foramen layers is varied.

Figure 23 shows a graphical representation of the data in Table 1.

The recorded stresses are shown in Table 2, below.

Table 2: Results of the cantilever bending test simulations, showing the highest recorded von Mises stress as the thickness of the areola and foramen layers is varied. Units are MPa, mesh size is 10mm.

von Mises stress

[MPa]

Foramen thickness

Areola offset	310mm	330mm	350mm
-50mm	4329	4008	3828
0	3597	3415	3237
+50mm	3032	2900	2760

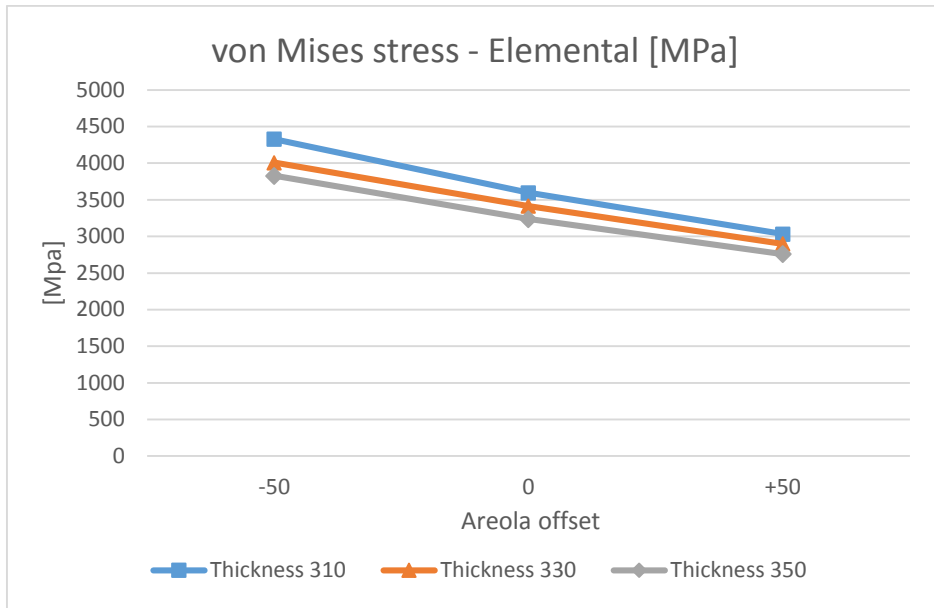


Figure 24: Graphical representation of the data in Table 2, showing the highest recorded von Mises stress in the cantilever bending test simulation as the thickness of the areola and foramen layers is varied.

Figure 23 and Figure 24 illustrate the results of the parameter study on the cantilever bending test. The required stiffness of the material increases as the thickness of the areola and/or foramen layers is reduced, and vice versa. The stresses exhibit a similar behavior.

3.5.2 Three-point-bending test

In the simulations of the three-point-bending test, the young's modulus was found to be 36685MPa. In the course of the parameter study, the calculated young's moduli varied from 28.8GPa to 47.5GPa, as seen in Table 3.

Table 3: Results of the three-point-bending test simulations, showing the young's modulus as the thickness of the areola and foramen layers is varied. Units are MPa, mesh size is 10mm.

Young's modulus

[MPa]

Foramen thickness

Areola offset	560mm	600mm	640mm
-50mm	46673	39725	34088
0	41914	35921	31041
+50mm	37395	32346	28127

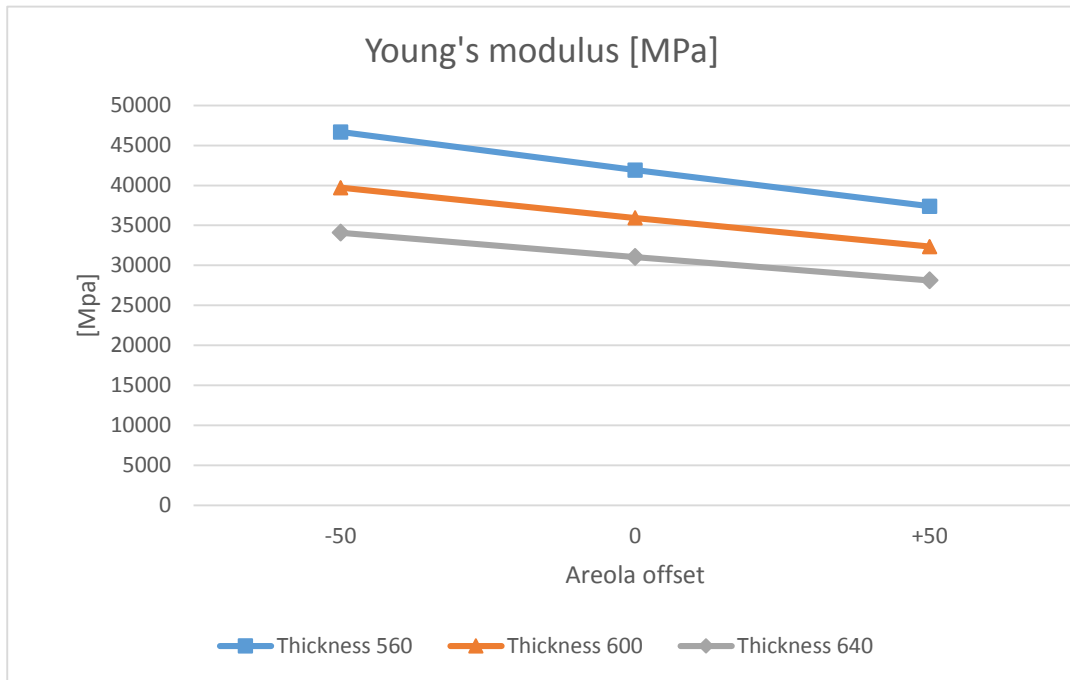


Figure 25: Graphical representation of the data in Table 3, showing the calculated young's modulus of the three-point-bending test specimen as the thickness of the areola and foramen layers is varied.

Table 4: Results of the three-point-bending test simulations, showing the highest recorded von Mises stress as the thickness of the areola and foramen layers is varied. Units are MPa, mesh size is 10mm.

von Mises stress

[MPa]

Foramen thickness

Areola offset	560mm	600mm	640mm
-50mm	2472	2138	1861
0	2939	2529	2211
+50mm	3247	2805	2487

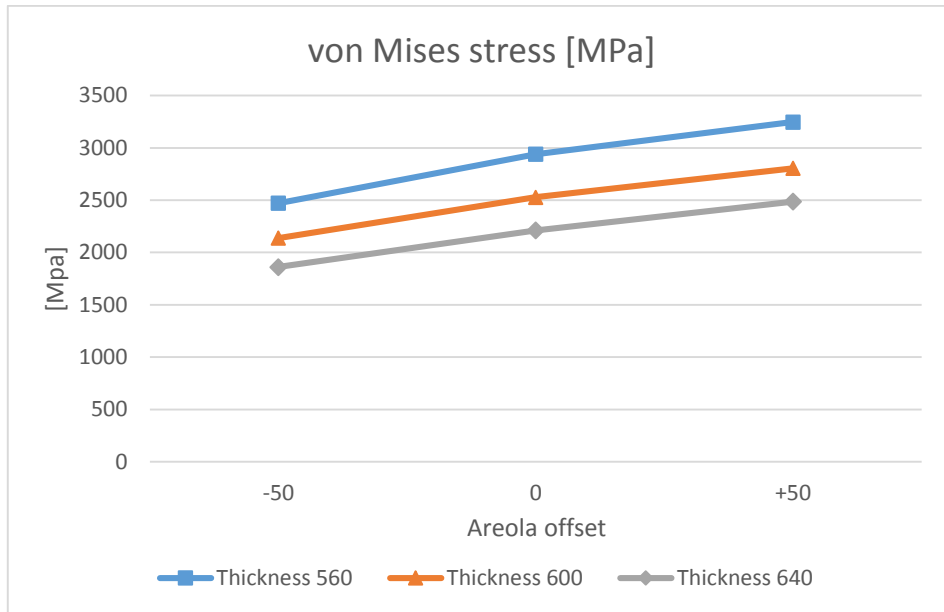


Figure 26: Graphical representation of the data in Table 4, showing the highest recorded von Mises stress in the three-point-bending test simulation as the thickness of the areola and foramen layers is varied.

Figure 25 and Figure 26 illustrate the results of the parameter study on the three-point-bending test. The required stiffness of the material increases as the thickness of the areola and/or foramen layers is reduced, and vice versa. The stress exhibits a different behavior than that of the cantilever bending test, increasing as the thickness of the areola layer is increased, and decreasing as the thickness of the foramen layer is increased.

3.5.3 Convergence

An attempt was made to refine the mesh so that the stress values would converge. However, refining the mesh led to increasing values for stress. As shown in Figure 27, the stress rose with each refining of the mesh.

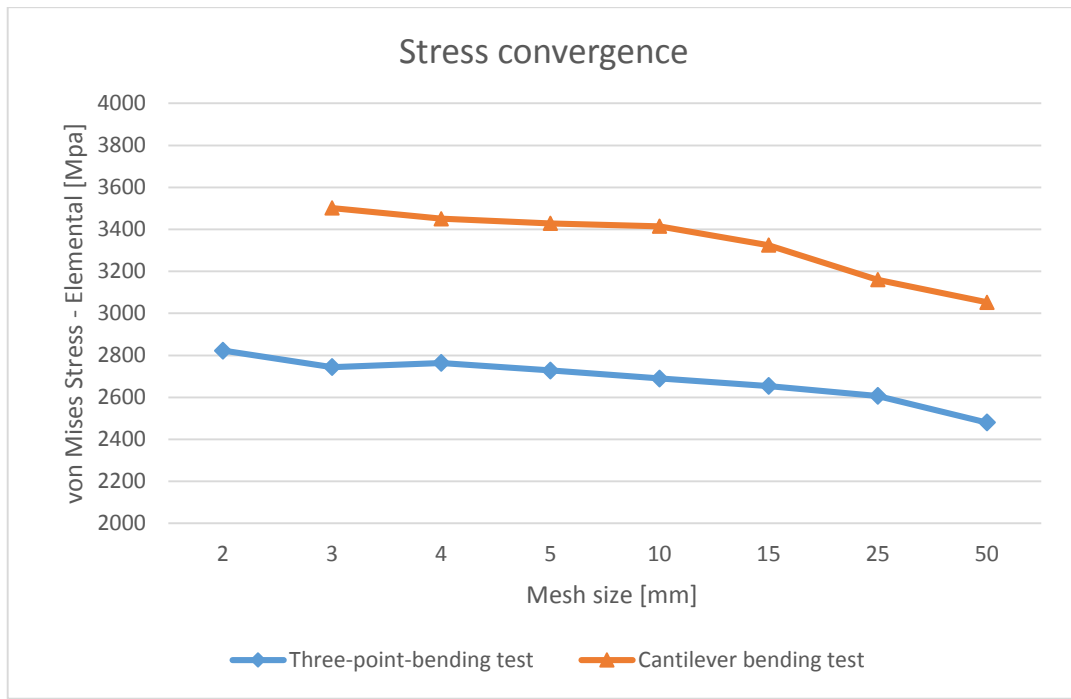


Figure 27: Stress values as function of mesh size. The reported stress values rose with each refinement of the mesh.

3.6 Discussion

The results presented in the previous section are based on simulations: approximations of reality. In this section, the various simplifications and assumptions that have been made, as well as the results obtained, are evaluated.

In this thesis, the results of two separate mechanical tests have been evaluated using FE-tools. These two simulations do not share any information, i.e. the results of one have not been applied to the other. The apparent proximity of the results, specifically of the calculated young's moduli, appear to support the validity of the results.

However, when creating models based solely on SEM-images of the specimens, it is highly unlikely to achieve a perfect reproduction of the physical specimens. In the case of the three-point-bending test, the placement of the load is also an uncertainty.

3.6.1 Cantilever bending test

The geometry of the cantilever bending test is partly based on SEM-images of the specimen, and partly on arbitrary approximations. By simulating the deformation of the beam without any supporting structure, the lower limit of the young's modulus was established to be 22.9GPa. However, some deformation in the surrounding structure was expected, and the supporting structure was added to the model. The specimen was milled from the center of the valve, from an area without pores. In this area, the areola walls seem to be more irregular than in the areas with pores. Hence, since the areola layer is mostly hidden in the SEM-images, the geometry of the supporting structure is extrapolated based on the visible geometry.

In the simulations, the load was applied to a circular area 300mm in diameter, i.e. half the radius of the indenter tip. The stresses surrounding the loaded area were low, as was the deformation of the loaded area. The size of this area was chosen based on the assumption that the specimen would conform slightly to the indenter tip.

3.6.2 Three-point-bending test

As with the CBT, the geometry of the TPBT is a matter of uncertainty. The model is based on images captured by S. H. Bjørnøy, showing the specimen from above and at a 52° tilt. There were no images showing the underside of the specimen. The shape of the specimen is also more complex than that of the CBT, especially along the outer perimeter of the foramen layer.

When modelling the underside of the specimen, the assumption was made that the only applicable geometry on the underside was the lips surrounding the pores. These lips were modelled as mirror images of their visible counterparts. However, the highest recorded stresses in the simulation do not coincide with the fracture in the specimen. One possible explanation for this is that there is a stress riser on the underside of the specimen not visible in the images. The highest recorded stresses are also lower than those in the CBT, which may support the theory that the sample did not fracture at the point suggested by the simulation.

The loaded area in the simulation does not coincide with the center of the sample holder or beam. The reasoning behind this is that the geometry of the indenter tip used in the testing prevents the tip from having reached the foramen layer before contacting the areola walls. It is therefore assumed that the tip was deflected by the areola walls into the pore near the center of the beam.

Another concern is the sample's position in the sample holder. The precise geometry of the sample holder is not visible in the images, and the sample holder itself appears to differ from the geometry described in S. H. Bjørnøy's master thesis. Since the precise distance between the supports can not be discerned, it is assumed that the sample holder is precise.

3.6.3 Young's modulus

In this thesis, the cantilever bending test and the three-point-bending test have yielded young's moduli of 32.8GPa and 36.7GPa, respectively. Comparing this to existing literature, the most comparable results are those found by Hamm & Merkel in 2001. That study found the young's modulus of the diatom silica to be 22.4GPa, which is comparable to the value found for the cantilever bending test without supporting structure; 22.9GPa.

However, considering the proximity of the results of the cantilever bending test and the three-point-bending test, the young's modulus appears to be higher than the findings of Hamm et al suggest. To decisively determine the young's modulus of the diatom silica, further tests should be performed and evaluated.

3.6.4 Ultimate strength

The simulations run on the cantilever bending test and the three-point-bending test returned von Mises stress figures of 3415MPa and 2690MPa, respectively. The highest reported stress in the cantilever bending test coincides with the point of fracture, as apparent from the SEM-images of the fractured specimen. The highest stress in the three-point-bending test, however, does not coincide with the point of fracture. This may support the results, in that the lowest of the reported stresses is not where the specimen fails. However, this signifies that the simulation does not correspond to the real test.

Comparing these results to existing literature, the most relevant study is again by Hamm et al. In this study, the highest stresses found were 640MPa. The difference may be partly attributed to a difference in mesh size. Hamm et al reports a mesh density of 350 elements per μm^3 , which is equivalent to a mesh size of approximately 140nm. As a finer mesh results in higher reported stresses, this comparatively coarse mesh would yield lower stress values. However, even when running the simulations in this thesis with a coarse mesh of 150nm, the resulting stress values were 2855MPa and 1511MPa for the CBT and TPBT, respectively.

Since the results found in this study rely only on two tests, this dataset is too small to determine the actual strength of the diatom silica. As such, further testing and evaluation is necessary.

3.7 Conclusion

The purpose of this thesis was to evaluate the mechanical properties of the diatom silica using FE-tools. Two separate mechanical tests performed at NTNU have been evaluated; a cantilever bending test and a three-point-bending test. The models were based on SEM-images of the samples before and after testing.

To determine the young's modulus of the samples, the simulations were first run under an assumed young's modulus. The young's modulus was then modified until the simulations yielded identical deformation as the real tests. The calculated young's moduli were 32.8GPa for the cantilever bending test and 36.7GPa for the three-point-bending test. Although these results differ from existing literature, the proximity of the results appear to support the validity of the simulations.

As for the mechanical strength of the material, the values returned from the simulations vary significantly. The highest recorded stress in the CBT simulation was 3415MPa, whereas the highest stresses in the TPBT simulation was 2690MPa. Furthermore, the area of highest stress in the TPBT does not coincide with the fracture in the sample.

With so small a dataset, it is difficult to draw any conclusions as to the physical properties of the material.

3.8 Further work

To more accurately determine the mechanical properties of the diatom silica, further studies must be done. Prior to testing, the geometry of the specimen must be thoroughly documented using SEM and AFM. By modelling the specimen prior to testing, simulations can be run to determine the appropriate load.

Hamm et al reported that several seconds elapsed before frustules fractured at set loads. By loading the samples with a predetermined load, one may be able to evaluate the creep properties of the material.

Referances

1. Gebeshuber, I. and R. Crawford, *Micromechanics in biogenic hydrated silica: hinges and interlocking devices in diatoms*. Proceedings of the Institution of Mechanical Engineers, Part J: Journal of Engineering Tribology, 2006. **220**(8): p. 787-796.
2. Hamm, C.E., et al., *Architecture and material properties of diatom shells provide effective mechanical protection*. Nature, 2003. **421**(6925): p. 841-843.
3. Gordon, R., et al., *The glass menagerie: diatoms for novel applications in nanotechnology*. Trends in biotechnology, 2009. **27**(2): p. 116-127.
4. Parkinson, J. and R. Gordon, *Beyond micromachining: the potential of diatoms*. Trends in biotechnology, 1999. **17**(5): p. 190-196.
5. Losic, D., et al., *Atomic force microscopy (AFM) characterisation of the porous silica nanostructure of two centric diatoms*. Journal of Porous Materials, 2007. **14**(1): p. 61-69.
6. Bjørnøy, S.H., *NANOMECHANICAL TESTING OF DIATOMS*, in *IPM*. 2012, NTNU: Trondheim.
7. Crosta, X., *Marine diatoms in polar and sub-polar environments and their application to Late Pleistocene paleoclimate reconstruction*, in *Iodp-Canada Summer School on Ocean and Climate Changes in Polar and Subpolar Environments*, G. StOnge, C. VeigaPires, and S. Solignac, Editors. 2011, Iop Publishing Ltd: Bristol.
8. Townley, H.E., A.R. Parker, and H. White-Cooper, *Exploitation of diatom frustules for nanotechnology: tethering active biomolecules*. Advanced Functional Materials, 2008. **18**(2): p. 369-374.
9. Lin, K.-C., et al., *Biogenic nanoporous silica-based sensor for enhanced electrochemical detection of cardiovascular biomarkers proteins*. Biosensors and Bioelectronics, 2010. **25**(10): p. 2336-2342.
10. Li, A., et al., *Multi-layer hierarchical array fabricated with diatom frustules for highly sensitive bio-detection applications*. Journal of Micromechanics and Microengineering, 2014. **24**(2): p. 025014.
11. Dolatabadi, J.E.N. and M. de la Guardia, *Applications of diatoms and silica nanotechnology in biosensing, drug and gene delivery, and formation of complex metal nanostructures*. TrAC Trends in Analytical Chemistry, 2011. **30**(9): p. 1538-1548.
12. Losic, D., et al., *Surface functionalisation of diatoms with dopamine modified iron-oxide nanoparticles: toward magnetically guided drug microcarriers with biologically derived morphologies*. Chemical Communications, 2010. **46**(34): p. 6323-6325.
13. Behkam, B. and M. Sitti, *Bacterial flagella-based propulsion and on/off motion control of microscale objects*. Applied Physics Letters, 2007. **90**(2): p. 023902.
14. Almqvist, N., et al., *Micromechanical and structural properties of a pennate diatom investigated by atomic force microscopy*. Journal of microscopy, 2001. **202**(3): p. 518-532.
15. Vebner, M.J., *Nanomechanical Testing of Diatoms*, in *IPM*. 2013, NTNU: Trondheim.

Appendix A - Scaling of geometry and loads

This appendage contains detailed calculations regarding the geometry scaling necessary to avoid an inherent limitation in Siemens NX 8.5, namely that the program will not register a nanoscale sketch as valid geometry. In order to avoid this limitation, the geometry was scaled such that nanometers were modelled as millimeters, i.e. a geometry scaling of 10^6 . The loads were scaled accordingly, resulting in that micronewtons were simulated as Meganewtons.

A.1 Normal stress and shear stress

The stress σ on a beam of dimensions $w \cdot h$ as a function of force is calculated as

$$\sigma = \frac{F}{A} = \frac{F}{w * h}$$

Scaling the geometry with a scale S will result in a scaling of the force. The scaled force, F_s , can be calculated as

$$\frac{F}{w * h} = \frac{F_s}{(w * S) * (h * S)}$$

As such, the scaled force F_s can be expressed as

$$F_s = F * S^2$$

The same is also true for shear stress, as the formulae are virtually identical.

A.2 Bending stress

The stresses σ_B in a beam with a rectangular cross section measuring $w \cdot h$ subjected to a force F at length L can be expressed as

$$\sigma_B = \frac{6 * F * L}{w * h^2}$$

Introducing the scale S , the formula can be expressed as

$$\frac{6 * F * L}{w * h^2} = \frac{6 * F_s * (S * L)}{(w * S) * (h * S)^2} = \frac{6 * F_s * L}{w * h^2 * S^2}$$

The scaled force F_s can then be expressed as

$$F_s = F * S^2$$

In this thesis, the geometry scale factor S is 10^6 , i.e. the loads must be scaled to 10^{12} to achieve correct results.

Appendix B - Modelling of Bjørnøy's H₂O₂ Beam 7

In this appendage, the process of creating the FE-model of Bjørnøy's H₂O₂ Beam 7 is described in detail. The model is based on SEM-images and measurements from S.H. Bjørnøy's master's thesis.

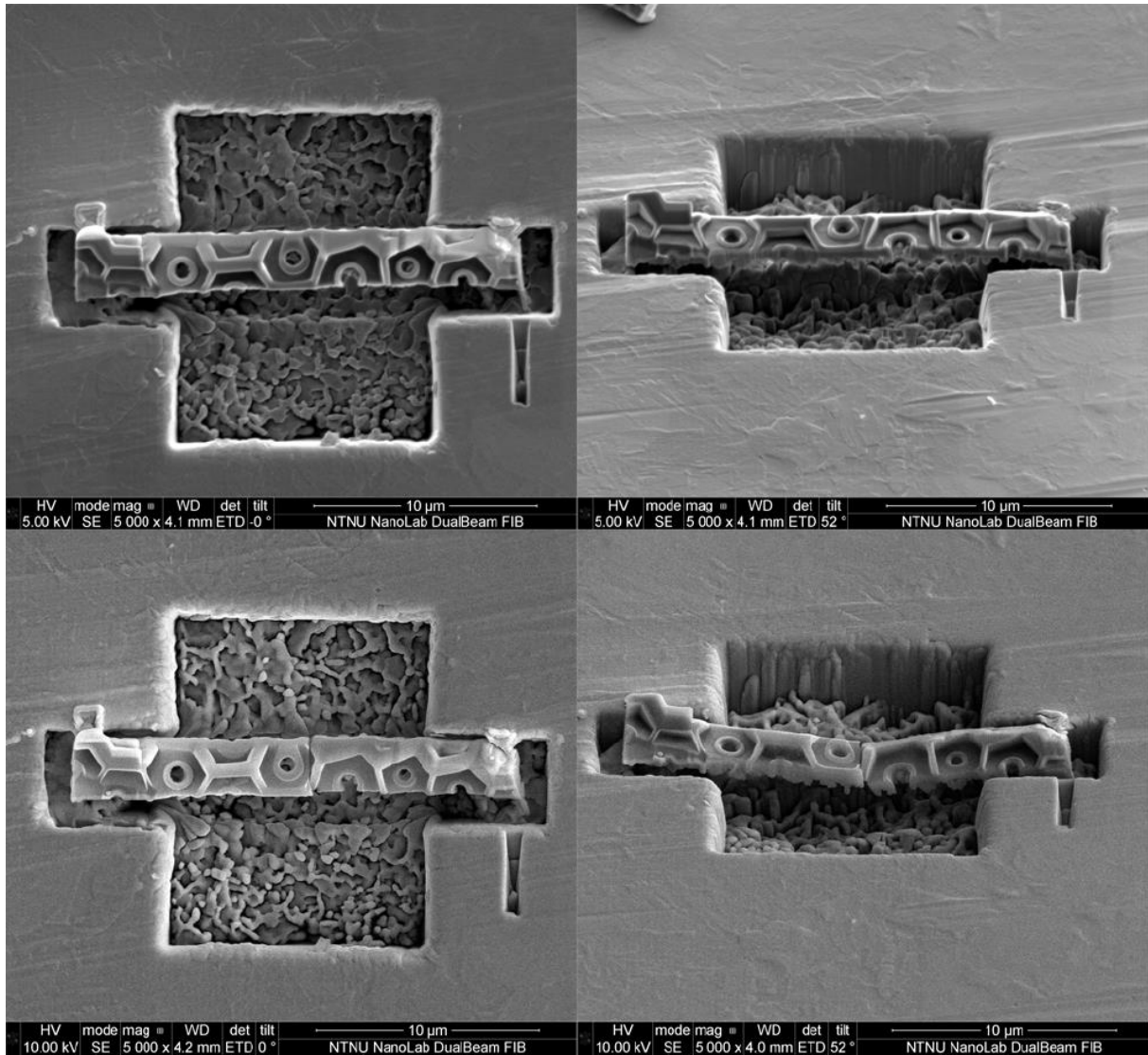


Figure 28: SEM-images of the beam before (top) and after (bottom) testing. The images are captured from above (left) and at a 52° tilt (right). The scale bar is 10µm. Images reproduced from S.H. Bjørnøy's master thesis.

The images in Figure 28 show the beam from above and at a 52° tilt before and after testing. These images form the basis for the FE-model used in the simulations.

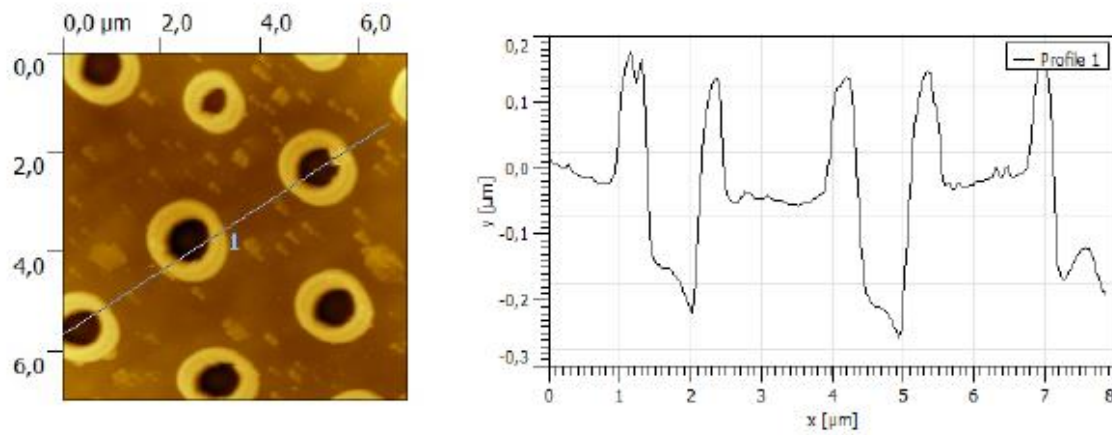


Figure 29: Image obtained by S.H. Bjørnøy using AFM. The "lips" around the pores are 150-180nm in height. Image taken from S.H. Bjørnøy's master thesis.

Figure 29 shows measurements taken using Atomic Force Microscopy (AFM) of the foramen layer. The lip around the pores in the foramen layer are 150-180nm in height.

Appendix C- Modelling of the Cantilever Beam Test Specimen

This appendage contains a systematic description of the procedure used to model the cantilever beam test (CBT). The FE-model was based on SEM-images and measurements provided by Christian Thaulow. These measurements include the thickness of the foramen layer, as well as the placing of the indenter tip.

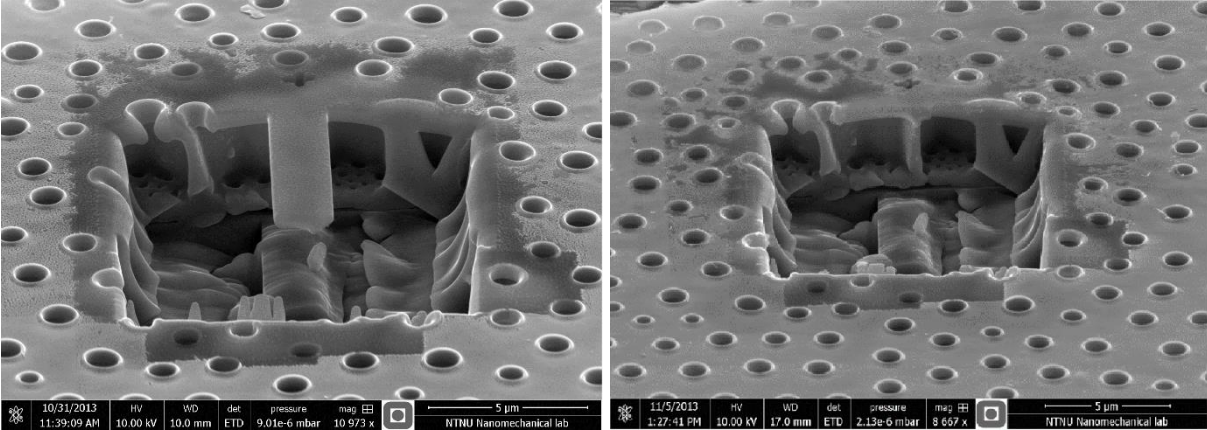


Figure 30: SEM-images of the CBT specimen before (left) and after testing (right).

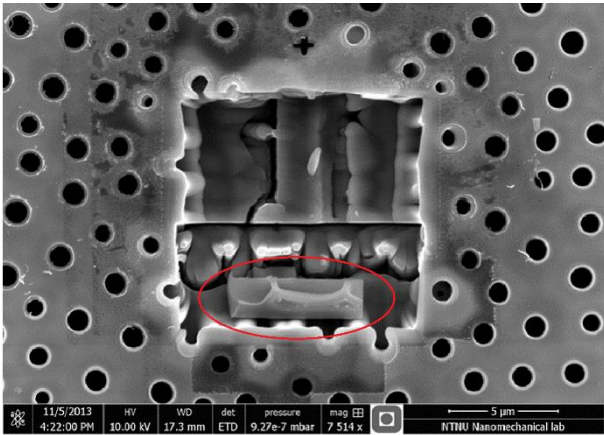


Figure 31: The fractured beam is visible (encircled) showing the geometry of the areola layer

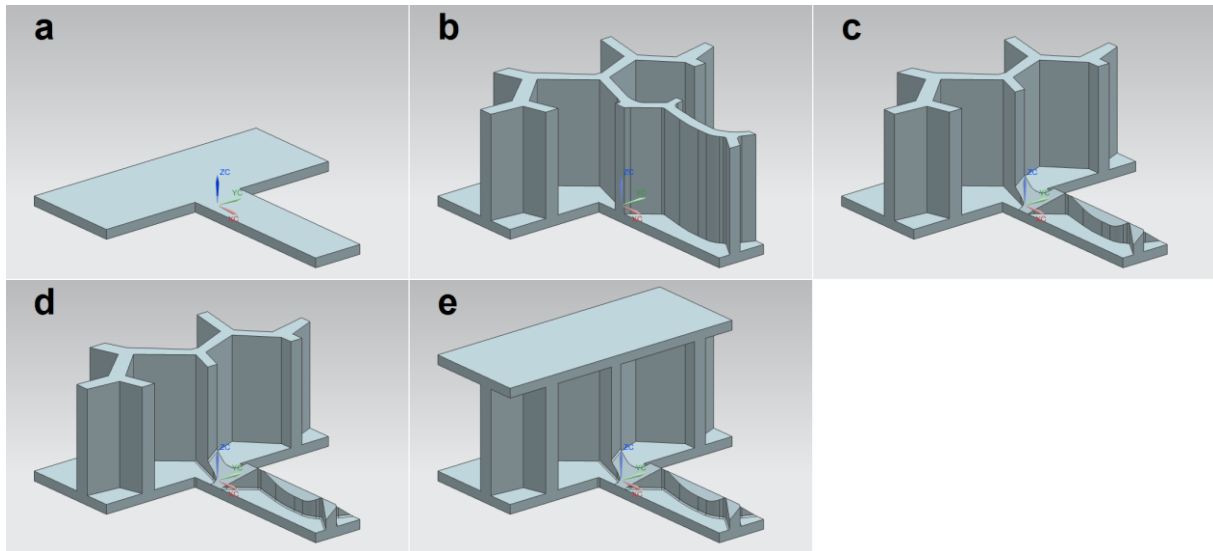


Figure 32: Sequential steps of the modeling process.

First, the outline of the foramen layer is established. As shown in Figure 31, the fractured beam is visible from below after testing. Using the scale bar on the image, the length and width of the beam was determined. To more accurately determine the stiffness of the structure, it was decided to include a section of the whole frustule. This section measure 2*5 times the width of the beam. Ref Figure 32a.

Using the image of the fractured beam in Figure 31, the contours of the areola layer was then sketched onto the foramen layer. The part of the areola visible in Figure 31 is sketched as accurately as possible, whereas the areola in the surrounding structure is based on the visible geometry in Figure 30. The height of the areola layer was estimated from Figure 30. Ref Figure 32b.

The areola layer on the beam is then trimmed to an angle of 52 degrees, the angle at which the areola layer is milled away with the Focused Ion Beam (FIB). This extruded cut extends the length of the beam only. Ref Figure 32c.

The transition from the areola to the foramen layers is rounded to 50nm to avoid stress risers. The exact curvature of this corner is not visible in the images, but it is assumed that the corner is curved to some extent. Ref Figure 32d.

Finally, the cribrum layer is added. This layer is for supporting the areola layer, and is modelled as the same thickness as the foramen layer. Ref Figure 32e.